Journal of Colloid and Interface Science 645 (2023) 33–44

Contents lists available at ScienceDirect

Journal of Colloid And Interface Science

journal homepage: www.elsevier.com/locate/jcis

Hollow porous carbon nanospheres containing polar cobalt sulfide (Co_9S_8) nanocrystals as electrocatalytic interlayers for the reutilization of polysulfide in lithium–sulfur batteries

Su Hyun Yang [a,1], Jang Min Choi [b,1], Rakesh Saroha [b], Sung Woo Cho [b], Yun Chan Kang [a,*], Jung Sang Cho [b,*]

[a] Department of Materials Science and Engineering, Korea University, Anam-Dong, Seongbuk-Gu, Seoul 136-713, Republic of Korea
[b] Department of Engineering Chemistry, Chungbuk National University, Chungbuk 361-763, Republic of Korea

HIGHLIGHTS

- Hollow porous carbon nanospheres (HPCNSs) are prepared.
- Comprising well-embedded metallic and polar cobalt sulfide (Co_9S_8) nanocrystals.
- Co_9S_8 nanocrystals act as chemisorption sites for efficient anchoring of polysulfide.
- Li–S cell with Co_9S_8@HPCNS-coated separator exhibits stable performance.

GRAPHICAL ABSTRACT

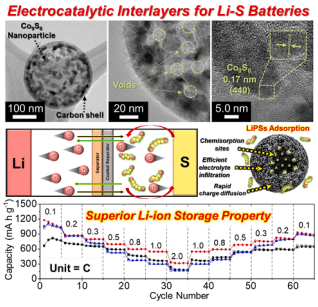

ARTICLE INFO

Keywords:
Hollow carbon nanosphere
Metal sulfide nanocrystal
Polysulfide capturing
Functional interlayer
Lithium–sulfur battery

ABSTRACT

Hypothesis: The introduction of functional interlayers for efficient anchoring of lithium polysulfides has received significant attention worldwide.
Experiments: A facile wet-chemical method was adopted to obtain hollow porous carbon nanospheres (HPCNSs) impregnated with metallic and polar cobalt sulfide (Co_9S_8) nanocrystals (abbreviated as "Co_9S_8@HPCNS"). The prepared nanocrystals were employed as electrocatalytic interlayers *via* separator coating for the efficient capture and reutilization of polysulfide species in Li-S batteries. The HPCNSs were synthesized *via* the polymerization method followed by carbonization and template removal. The Co_9S_8 nanocrystals were impregnated inside the HPCNSs, followed by heat treatment in a reducing atmosphere.
Findings: The porous structure of the CNS enables the efficient percolation of the electrolyte, in addition to accommodating unwanted volume fluctuations during redox processes. Furthermore, the metallic Co_9S_8 nanocrystals improve the electronic conductivity and enhance the polarity of the CNS towards the polysulfide.

Abbreviations: Co9S8, cobalt sulfide; CNSs, carbon nanosphere; Li–S, lithium–sulfur; TEOS, tetraethyl orthosilicate; TEM, transmission electron microscopy; XRD, X-ray diffraction; TGA, thermogravimetric analysis; EIS, electrochemical impedance spectroscopy; HPCNs, hollow porous carbon nanospheres; F-CNSs, filled carbon nanospheres; LSBs, lithium sulfur batteries; SEM, scanning electron microscopy; HR-TEM, high resolution TEM; BET, Brunauer–Emmett–Teller; XPS, X-ray photoelectron spectroscopy.

* Corresponding authors.
E-mail addresses: yckang@korea.ac.kr (Y.C. Kang), jscho@cbnu.ac.kr (J.S. Cho).
[1] These authors contributed equally.

https://doi.org/10.1016/j.jcis.2023.04.083
Received 11 January 2023; Received in revised form 12 April 2023; Accepted 19 April 2023
Available online 28 April 2023

Correspondingly, the Li–S cells featuring Co_9S_8@HPCNS as electrocatalytic interlayers and regular sulfur (S) electrodes display improved electrochemical performance such as reasonable rate performance and prolonged cycling stability at different current rates (0.1, 0.5, and 1.0 C). Therefore, we anticipate that the rational design strategy proposed herein will provide significant insights into the synthesis of advanced materials for various energy storage applications.

1. Introduction

Li-S batteries have been considered as a suitable alternative to the currently available Li-ion batteries owing to their high theoretical discharge capacity (1675 mA h g^{-1}), nominal average discharge voltage (2.1 V *vs.* Li^+/Li), and low production cost because of the widespread availability of elemental S [1–6]. However, owing to the insulating nature of S and its end discharge product (lithium sulfide; Li_2S), polysulfide (Li_2S_x; $x = 8$, 6, and 4) shuttling, volume fluctuations (due to the density difference between S and Li_2S), and Li instability, the practical application of lithium-sulfur batteries (LSBs) is hindered [7–12]. These issues result in low active-material utilization, poor reaction kinetics, inferior rate capabilities, unstable cycling performances, low Coulombic efficiencies, and poor anode safety [13–16].

To address the aforementioned drawbacks, the interlayer strategy has attracted worldwide attention in the last few years to suppress the polysulfide crossover and improve the overall electrochemical performance. The interlayer is commonly fabricated *via* a commercial separator coating or as a freestanding disk. To qualify as an interlayer material, the nanostructure must possess a few intrinsic characteristics, such as high porosity, high conductivity, and the presence of polar materials [17]. The porosity facilitates the inhibition of electrode pulverization caused by undesired volume variations in S and Li_2S during the redox processes. In addition, the porous nanostructure ensures an adequate diffusion of charged species along with efficient electrolyte percolation [18]. To introduce porosity inside the nanostructures, various techniques have been developed, which mainly include generating either template-derived or template-free pores [19]. In general, template-derived pores are obtained using either a hard or a soft template. The hard template method involves the removal of cavity-filling precursors after synthesis, whereas the soft template method facilitates more subtle interactions between the template and framework source, thereby offering good control of the porosity [20].

The presence of a polar material is another desired characteristic for ensuring the efficient capture and electrocatalytic conversion of the polysulfide species, resulting in high active material utilization. Numerous materials have been previously evaluated as efficient interlayer materials, including conductive carbon skeletons [21–23], metal oxides [24,25], metal nitrides [26], and metal selenides [27,28], and many more [29–32]. In particular, transition metal sulfides have been extensively explored owing to their excellent polysulfide anchoring capabilities [27]. In addition, compared with those of metal oxides, the metallic characteristics of metal sulfides facilitate fast electron transfer thus allowing kinetically favored electrocatalytic conversion of polysulfides [33].

Based on the above discussion, we herein synthesized hollow porous carbon nanospheres (HPCNSs) comprising well-embedded metallic and polar Co_9S_8 nanocrystals (abbreviated as Co_9S_8@HPCNS) and utilized them as a multifunctional interlayer in Li-S cells by pairing with elemental S electrodes to improve the electrochemical performance. Initially, the HPCNS sample was prepared *via* facile polymerization followed by carbonization and template removal. Subsequently, the Co_9S_8 nanocrystals were impregnated inside the HPCNS. The as-prepared Co_9S_8@HPCNS sample was then used as a multifunctional and electrocatalytic interlayer for highly stable LSBs. The hollow structure or cavity was derived *via* template removal (silica (SiO_2) in the present case) strategy. The hollow structure facilitates efficient electrolyte penetration and channelizes undesired volume variations during the redox processes. Similarly, metallic and polar Co_9S_8 nanocrystals act as chemisorption sites for effective polysulfide anchoring and catalytic conversion. To the best of our knowledge, the use of the above-mentioned nanostructure with commendable structural merits such as inner hollow space and a large surface area along with well-grafted metallic metal sulfide nanocrystals as a polysulfide barrier in Li-S cells has not been reported thus far.

Owing to the structural advantages, the Li-S cells employing Co_9S_8@HPCNS-coated separator and regular S electrode displayed an improved electrochemical performance such as sufficient rate capability and extended cycling properties at various current rates, owing to the improved active material utilization.

2. Materials and methods

2.1. Chemicals

All the chemicals used in the synthesis were of analytical grade *viz.* tetraethyl orthosilicate (TEOS, 95.0%, SAMCHUN), ammonia water (28.0–30.0%, SAMCHUN), resorcinol (98.0%, SAMCHUN), formaldehyde solution (36.0–38.0%, JUNSEI), sodium hydroxide (NaOH, 97.0%, JUNSEI), thiourea (98%, JUNSEI) and $Co(NO_3)_2{\cdot}6H_2O$ (97%, SAMCHUN). The impregnation solution was prepared using high-purity ethanol (99.9%, SAMCHUN).

2.2. Synthesis of Co_9S_8@HPCNS

The hollow porous carbon nanospheres with well-grafted metal sulfide nanocrystals (denoted as Co_9S_8@HPCNS) samples were prepared *via* facile impregnation method followed by heat treatment. Initially, HPCNS was synthesized using a wet chemical method. Briefly, 3.46 mL of TEOS (Tetraethyl orthosilicate) and 3.5 mL of ammonia water were added to a mixture containing 70 mL of high-purity ethanol and 10 mL of deionized (DI) water using stirring. Subsequently, 0.4 g of resorcinol and 0.56 mL of formaldehyde solution were added to the above-formed silica precursor solution with vigorous stirring for 24 h. The precipitates were then centrifuged with ethanol and DI water. To prepare the SiO_2@SiO_2/C nanospheres, the precipitates were heat treated at 700 °C in an Ar gas atmosphere for 5 h at a ramp rate of 2 ℃ min^{-1}. Subsequently, the SiO_2@SiO_2/C nanospheres were etched using a 4 M NaOH solution through a hydrothermal process at 130 °C for 6 h. After cooling to ambient temperature, the contents were washed with a mixture of DI water and ethanol and dried in a vacuum oven. The dried sample (0.02 g) was impregnated in a high-purity ethanol solution containing Co $(NO_3)_2{\cdot}6H_2O$ (0.137 mmol) and thiourea (0.415 mmol). Subsequently, the impregnated HPCNS powders were heat-treated in a tube furnace under H_2/Ar (10/90 wt%) gas atmosphere at 350 °C for 6 h using a ramping rate of 5 °C min^{-1} to form the Co_9S_8@HPCNS powder. For comparison, filled carbon nanospheres (F-CNSs) were also synthesized using the same process except for the addition of TEOS, which is a pore-forming generator. However, to obtain a size comparable to that of HPCNS, the amount of reagents used was controlled as follows: 3.5 mL of ammonia water, 0.2 g of resorcinol, and 0.28 mL of formaldehyde solution. Subsequently, these reagents were added to a solution containing 70 mL of high-purity ethanol and 10 mL of DI water. Additionally, pristine Co_9S_8 sample was also prepared as a control by simply mixing fixed proportions of cobalt nitrate and thiourea followed by identical heat-treatment conditions.

2.3. Characterizations of materials

The morphologies of Co_9S_8@HPCNS, HPCNS, and F-CNS were confirmed using microscopic characterization techniques such as scanning electron microscopy (SEM, VEGA3 SBH) and field-emission transmission electron microscopy (FE-TEM, JEM-2100F). X-ray photoelectron spectroscopy (XPS, Thermo Scientific K-Alpha) was conducted to confirm the chemical bonding of Co_9S_8@HPCNS at Sunchun National University Center for Research Facilities. The crystal phases of the prepared samples were characterized by powder X-ray diffraction (XRD, X'Pert PRO) with Cu-Kα radiation (λ = 1.5418 Å) at the Korea Basic Science Institute. The surface areas and pore sizes were investigated using the Brunauer–Emmett–Teller (BET) method using pure N_2 as the adsorbate gas. Thermogravimetric analysis (TGA) was performed using a Pyris 1 TGA (Perkin Elmer) in the 30–700 °C range at a ramp rate of 10 °C·min^{-1} in air to confirm the carbon content of the composites. Raman spectroscopy (Jobin Yvon LabRamHR800, excited by a 632.8-nm-wavelength He/Ne laser) was performed for analyzing the structure of the carbon present in the Co_9S_8@HPCNS sample.

2.4. Cell assembly and electrochemical characterization

The multifunctional interlayers were obtained using a typical slurry coating technique. Briefly, the as-prepared Co_9S_8@HPCNS sample (70 wt%), super-P (20 wt%), and polyvinylidene fluoride (PVDF; 10 wt%) binder were dispersed in an optimal amount of *N*-methyl-2-pyrrolidone (NMP) solvent. The uniform slurry was coated onto a commercial polypropylene separator and dried subsequently at 60 ℃ overnight. Round discs (ϕ = 19 mm) were punched with an average loading of 0.5 mg cm^{-2}. Likewise, regular S electrodes were also prepared using an identical slurry process where elemental S, super-P, and PVDF were mixed in 7:2:1 mass ratio. The active S loading was fixed at 1.6 mg cm^{-2} (ϕ = 14 mm) throughout the experiments. The CR2032 coin cells were assembled using metallic-Li as the anode, regular S electrode as the cathode, and Co_9S_8@HPCNS-coated separator as the function interlayer. The electrolyte used was 1.0 M lithium bis(trifluoromethanesulfonyl) imide in 1,3-dioxolane (DOL) and 1,2-dimethoxyethane (DME) (1:1, v/v) with 0.5 M lithium nitrate ($LiNO_3$) as an additive. The electrolyte volume was fixed at 50 μL. The charge–discharge voltage profiles were observed at various current rates (C-rates) ranging from 0.1 to 2.0 C (1 C was equated to 1675 mA h g^{-1}). The cycling performance was also evaluated at 0.1 and 1.0 C rates. The cyclic voltammetry (CV) curves were obtained at various voltage scan rates from 0.05 to 0.5 mV s^{-1} in the voltage window of 1.7–2.8 V. The charge transfer characteristics were observed by Nyquist plots using an electrochemical impedance analyzer (ZIVE SP2; WonATech) coupled with an AC pulse of amplitude 5 mV in the frequency range of 10 mHz to 1 MHz. All the electrochemical tests were performed at ambient conditions using a WBCS3000 (WonATech) battery cycler.

2.5. Visual polysulfide adsorption and electrocatalytic conversion tests

Visual tests for demonstrating the polysulfide anchoring by the as-prepared samples were also performed. Briefly, elemental sulfur powder (S, Sigma-Aldrich, 99.98%) and Li_2S (≥99%, Sigma-Aldrich) were dispersed (5:1 M ratio) in DOL/DME (1:1, v/v) to produce a dark brown Li_2S_6 solution. Afterward, 1.0 mM Li_2S_6 solution was prepared in DOL/DME solvent and dropped into three glass vials having as-prepared nanospheres (3.0 mg each). A standard polysulfide solution was also prepared for comparison. Furthermore, symmetrical cells were made to determine the catalytic effect of the as-prepared nanospheres by using the prepared polysulfide solution. The counter and working electrodes (obtained using the slurry method) were kept identical and separated using a Celgard separator. CV plots were obtained for assembled symmetrical cells at a voltage scan rate of 3.0 mV s^{-1} in a voltage range of –1.0 to 1.0 V.

3. Results and discussion

3.1. Physical characterization results

The detailed formation mechanism of the Co_9S_8@HPCNS sample is illustrated in Scheme 1. First, carbon nanospheres with a well-formed cavity (HPCNSs) were obtained *via* a simple wet-chemical route involving facile polymerization followed by carbonization and template removal. The TEOS acts as a source for the formation of SiO_2-primary particle as well as the SiO_2-core particle whereas the formaldehyde-resorcinol solution undergoes a polymerization process and finally gets condensed onto the SiO_2-core particles. Additionally, the formaldehyde-resorcinol solution serves as a source of carbon precursor. The precipitates were centrifuged, collected, and washed repeatedly with ethanol and DI water. The carbonization process at 700 ℃ resulted in the conversion of formaldehyde-resorcinol matrix to an amorphous carbon nanosphere containing well-embedded TEOS-derived SiO_2-primary as well as the SiO_2-core particles (SiO_2@SiO_2/C). The HPCNS were obtained from SiO_2@SiO_2/C nanospheres *via* an etching process using 4 M NaOH solution and act as a reservoir for cobalt sulfide nanocrystals (Scheme 1-①). The etching removed both the SiO_2-primary and SiO_2-core particles, thereby forming mesopores and a central void or hollow inner space, respectively. A homogeneous solution containing cobalt nitrate and thiourea in ethyl alcohol was fully impregnated into the HPCNSs *via* a drop-and-dry method (Scheme 1-②). During this process, the solution can easily penetrate the central void through the well-developed mesopores of the HPCNSs with the aid of capillary action. Subsequently, the impregnated HPCNSs were heat treated in the H_2/Ar gas atmosphere at 350 °C for 6 h. During this process, the cobalt nitrate and thiourea reagents were converted into Co_9S_8 nanoparticles by reacting with H_2 gas and aggregated into an inner void *via* Ostwald ripening, resulting in the formation of Co_9S_8@HPCNS (Scheme 1-③) [34].

The material characteristics of the composites obtained at each step were investigated using various analytical techniques. The scanning electron microscopy (SEM) and transmission electron microscopy (TEM) images in Fig. S1a and b show that HPCNSs exhibit a uniform size distribution with an average diameter of 280 nm. The presence of multiple mesopores (Fig. S1b) and a large inner void with a carbon shell (thickness of 12 nm) are also observed. The mesopores serve as storage passages for the metal precursor and thiourea. After impregnation, the morphology of the HPCNS infiltrated with cobalt nitrate and thiourea reagents changes negligibly and no aggregation is observed, suggesting that the reagents have infiltrated the HPCNS template (Fig. S2). Furthermore, the overall morphologies of Co_9S_8@HPCNS obtained after heat treatment do not change significantly (Fig. S3). However, the TEM images indicate that the Co_9S_8 nanoparticles (black region) aggregate into HPCNSs (Fig. 1a and b). In addition, mesoporous voids (highlighted by circles; Fig. 1b) are also observed owing to the etching of SiO_2-primary particles. The high-resolution TEM (HR-TEM) image in Fig. 1c shows a clear lattice spacing of 0.17 nm corresponding to the (4 4 0) crystal plane of Co_9S_8 nanoparticles that are well grafted into the carbon matrix. The selected area electron diffraction (SAED) pattern (Fig. 1d) also reveals well-resolved diffraction ring patterns corresponding to the (3 1 1), (4 0 0), (5 1 1), (4 4 0), and (7 3 1) planes of the Co_9S_8 phase and is consistent with the corresponding XRD results presented in Fig. 1e. The distribution of Co and S shows that cobalt sulfide exists only in the internal space of the HPCNS (Fig. 1f). To validate the structural advantages of Co_9S_8@HPCNS, F-CNSs were also prepared using the same process except for the addition of a pore-forming agent (TEOS). The as-prepared F-CNS sample exhibits a filled structure with a uniform size distribution (average diameter of 250 nm), as shown in the SEM image (Fig. S4a). The TEM image in Fig. S4b further validates the SEM results, indicating filled-type morphology primarily due to the absence of mesoporous voids formed from etched SiO_2-primary particles. Furthermore, SEM results of the pristine Co_9S_8 sample in Fig. S5a reveal particle-type

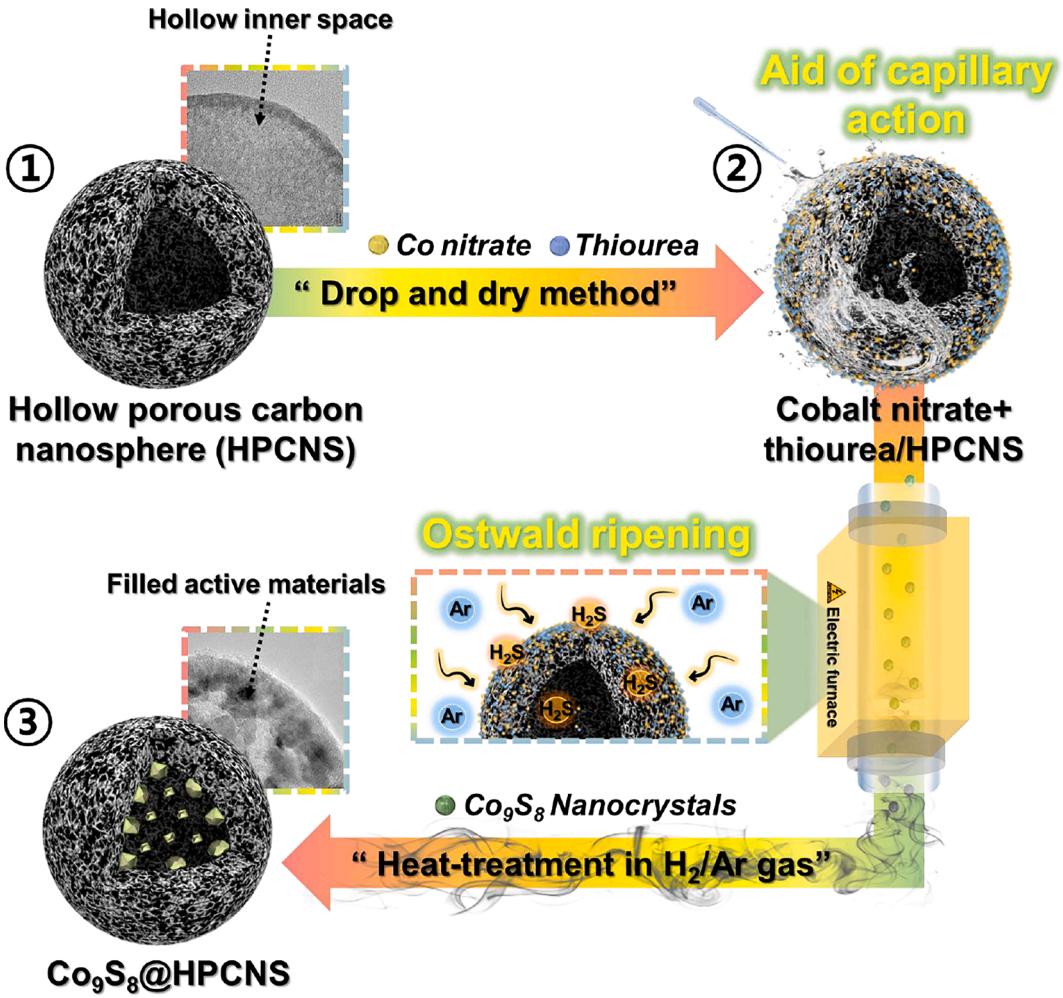

Scheme 1. The detailed synthesis mechanism of hollow porous carbon nanospheres with well-grafted metal sulfide nanocrystals (Co_9S_8@HPCNS).

morphology with high degree of agglomeration. The XRD peaks in Fig. S5b are indexed to the cubic phase of Co_9S_8 crystal structure.

The chemical composition of the Co_9S_8@HPCNS was determined *via* X-ray photoelectron spectroscopy (XPS; Fig. 2). The survey spectrum of Co_9S_8@HPCNS indicates the presence of Co, S, C, and O, which agrees well with the elemental mapping results. The presence of O was attributed to surface oxidation during sample preparation. The Co 2p spectrum in Fig. 2b shows several peaks corresponding to Co^{2+} bonding (778.5 and 794.3 eV) and Co^{3+} bonding (781.2 and 797.4 eV), along with satellite peaks (denoted as Sat.), all of which are associated with Co_9S_8 nanocrystals and partially oxidized cobalt sulfides, such as cobalt sulfate [35–39]. The S 2p spectrum in Fig. 2c shows five peaks at 161.4, 162.6, 163.9, 165.1, and 168.6 eV. The two peaks at 161.4 and 162.6 eV match well with the binding energies of S $2p_{3/2}$ and S $2p_{1/2}$, respectively [40,41]. The presence of C—S (163.9 eV) and C═S (165.1 eV) is attributed to the interfaces between Co_9S_8 and the carbon spheres [40]. The peak at 168.6 eV is attributed to the S—O bond of a partially oxidized sulfur species on the surface of Co_9S_8@HPCNS [42]. The deconvoluted C 1s spectrum (Fig. 2d) exhibits four well-fitted peaks at 284.5, 285.0, 285.8, and 288.8 eV, which correspond to the C═C sp^2, C—C sp^3, C—S, and C═O bonds, respectively [43–46]. The appearance of the highest-intensity peak corresponding to the C═C bond firmly indicates the existence of carbonaceous species in the prepared samples.

To confirm the thermal behavior and quantify the carbon content in Co_9S_8@HPCNS, thermogravimetric analysis (TGA) was performed. In Fig. 3a, the initial weight loss upon increasing the temperature from 100 to 150 ℃ is attributed to the evaporation of adsorbed water in the structure. The slight weight increase upon increasing the temperature from 200 to 370 ℃ is related to the partial oxidation of cobalt sulfide to cobalt sulfate [47]. Furthermore, the weight loss above 400–460 ℃ is associated with carbon combustion and the formation of cobalt oxide. Based on the TGA data, the calculated carbon content in Co_9S_8@HPCNS was 54.5%. To further confirm the carbon properties, Raman spectroscopy was conducted, and the results are shown in Fig. 3b. The two broad peaks positioned at approximately 1342 and 1591 cm^{-1} for Co_9S_8@HPCNS correspond to the D- and G-bands of carbonaceous materials, respectively [48]. The D and G peak intensity ratio (I_D/I_G) of 0.86 indicates that the HPCNSs possess few defects [11]. The Brunauer–Emmett–Teller (BET) analysis shows that the specific surface areas of Co_9S_8@HPCNS, HPCNS, and F-CNS are 291.7, 538.8, and 307.8 $m^2\ g^{-1}$, respectively (Fig. 3c). In contrast to HPCNS, the decreased surface area and pore volume of the Co_9S_8@HPCNS composite demonstrate that metal sulfides are well embedded in HPCNS. The large specific surface area of F-CNS is attributed to the formation of micropores when organic matter is converted into carbon during the heat treatment [49]. The Barrett–Joyner–Halenda (BJH) pore size distributions of Co_9S_8@HPCNS and HPCNS (Fig. 3d) exhibit a narrow pore size in the range of 4–6 nm, suggesting the presence of mesopores. These results match well with the results presented in Fig. 1 and Fig. S1. The mesopores facilitated electrolyte percolation and channeled volume perturbations during the redox process, thereby improving the overall electrochemical performance.

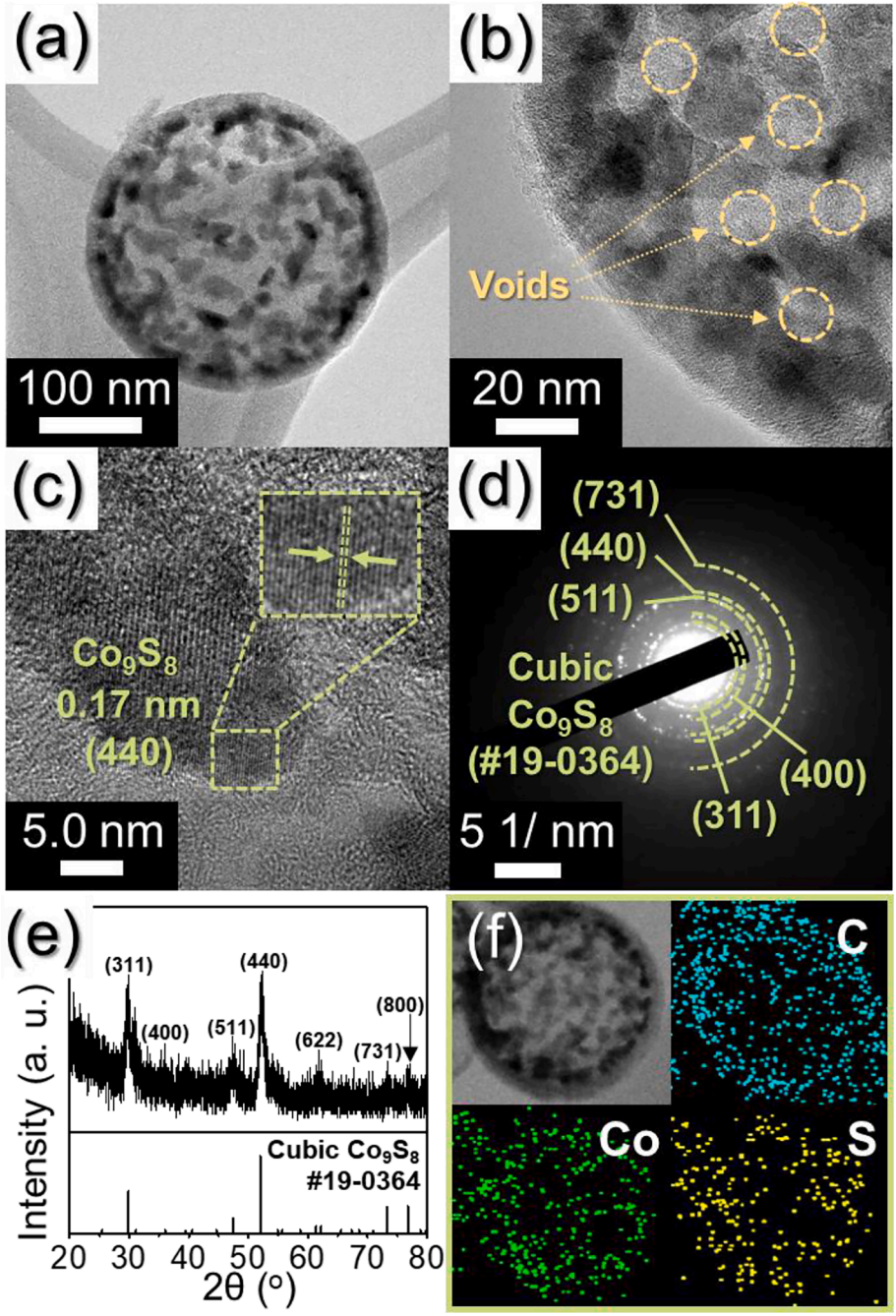

Fig. 1. Morphologies, SAED, XRD, and elemental mapping images of Co_9S_8@HPCNS: (a, b) TEM images, (c) HR-TEM image, (d) SAED pattern, (e) XRD pattern, and (f) elemental mapping images.

3.2. Electrochemical results

Before electrochemical testing, the physical attributes of the coated separators were examined. A digital image of the coated separator after drying at 60 °C (Fig. S6a) indicates a uniform crack-free coating. Circular disks (ϕ = 19 mm) were punched from the coated separator as multifunctional interlayers (Fig. S6b). The thicknesses of the various coated separator disks and the pristine separator were measured using a digital meter (Fig. S6c–f), revealing a coating thickness of 15 μm. The folding and twisting of the coated separator disks shown in Fig. S6g firmly indicate the high mechanical integrity of the interlayer. The SEM micrograph of the F-CNS-coated separator shown in Fig. S7a shows porous openings that facilitate Li-ion diffusion. The SEM micrograph of the Co_9S_8@HPCNS-coated separator shown in Fig. S7b indicates a uniform coating of the Co_9S_8@HPCNS sample along with super-P. In addition, the cross-sectional image in Fig. S7c suggests a uniform coating thickness of 15 μm, which matches the results described in Fig. S6c–e.

The results of the electrochemical tests performed on various Li–S cells using coated separators are shown in Fig. 4. The cyclic voltammetry (CV) curves obtained at a voltage ramp rate of 0.1 mV s^{-1} in the voltage range of 1.7–2.8 V are shown in Fig. 4a. The Co_9S_8@HPCNS-coated separator exhibits sharp and well-resolved redox peaks compared to the HPCNS-coated and F-CNS-coated separators. The reduction peak pair at 2.29/1.99 V observed for the Co_9S_8@HPCNS-coated separator indicates a reduction of higher-order polysulfide species to middle- and lower-order polysulfide molecules to finally form Li_2S. Similarly, the appearance of closely spaced peaks at 2.39 and 2.43 V signifies the oxidation of

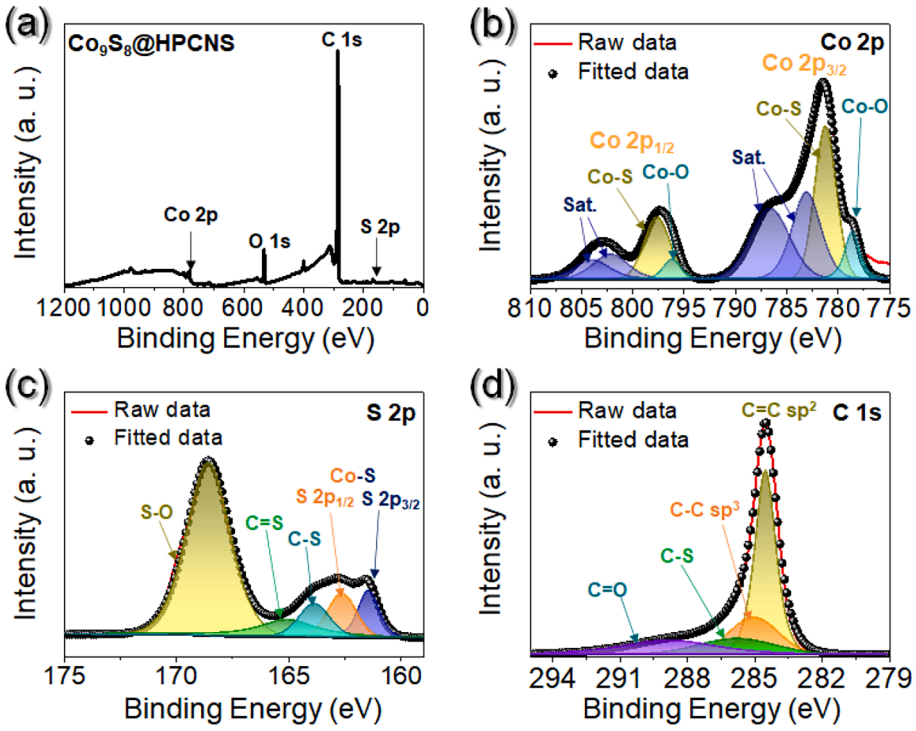

Fig. 2. XPS spectra of Co_9S_8@HPCNS: (a) survey scan, (b) Co 2p, (c) S 2p, and (d) C 1s spectrum.

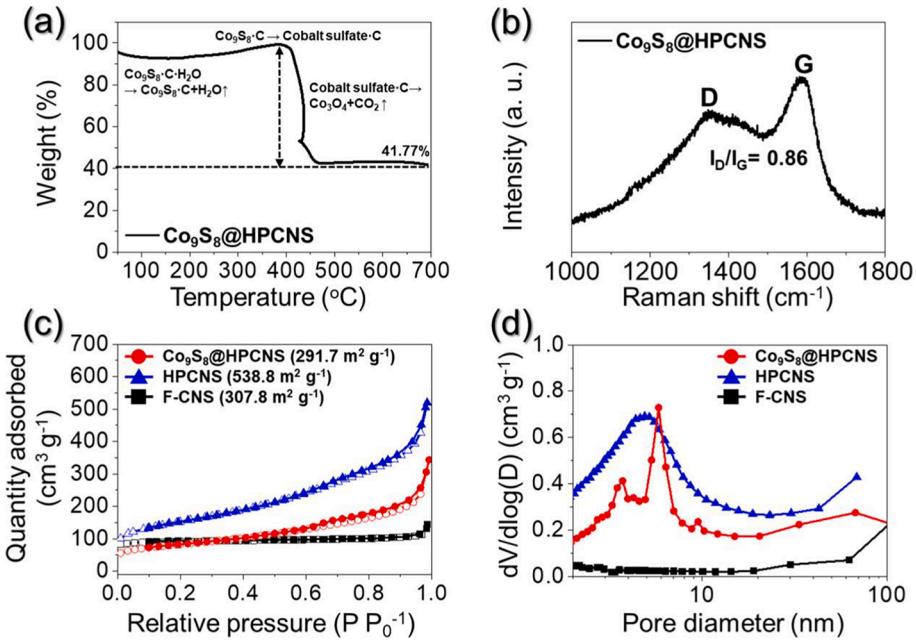

Fig. 3. Characteristics of Co_9S_8@HPCNS: (a) TG curve, (b) Raman spectrum, (c) N_2 adsorption and desorption isotherms, and (d) BJH pore size distributions with HPCNS and F-CNS.

Li_2S to elemental S *via* middle- and higher-order polysulfide species. The cells featuring HPCNS-coated and F-CNS-coated separators also displayed typical redox processes involving only S and Li_2S. However, the low redox current intensities of the HPCNS-coated separator and the lowest value observed for the F-CNS-coated separator indicated poor redox kinetics inside the cell. This observation was significantly pronounced when the polarization effect was considered. For instance, the Co_9S_8@HPCNS-coated separator exhibited the lowest polarization potential ($\Delta V = 130$ mV) compared to that of the HPCNS-coated ($\Delta V = 180$ mV) and F-CNS-coated separators ($\Delta V = 230$ mV). Furthermore, the initial five CV cycles for all separator arrangements are shown in Fig. S8a–c, indicating almost overlapping profiles. However, the disparity in the redox peak intensities suggests different discharge capacities. The initial charge–discharge voltage profile is plotted to verify the CV observations, as shown in Fig. 4b. The cells utilizing the Co_9S_8@HPCNS-coated and HPCNS-coated separators display well-distinguished voltage plateaus, which are well synchronized with the CV results. Additionally, the long voltage plateau suggests kinetically favored electrochemical processes. In contrast, the cell featuring the F-CNS-coated separator exhibits a lower voltage plateau. Correspondingly,

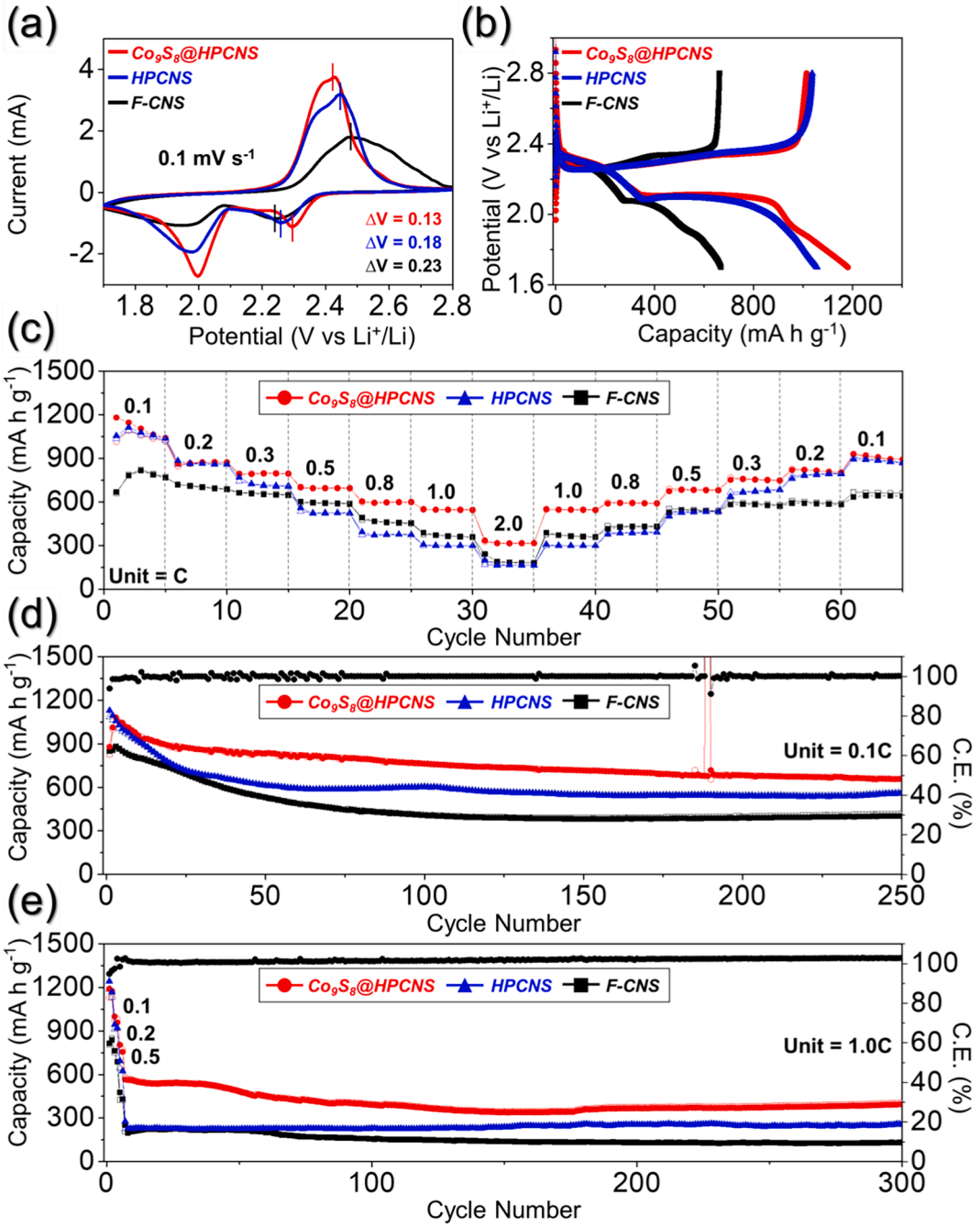

Fig. 4. Electrochemical performances of Li–S cells assembled with different interlayer arrangements: (a) cyclic voltammetry curves for first cycle at 0.1 mV s^{-1}, (b) initial charge–discharge voltage profile at 0.1 C, (c) rate capability tests at various current rates and cycling performance at 0.1 C (d) and 1.0 C (e).

the cells utilizing Co_9S_8@HPCNS-coated, HPCNS-coated, and F-CNS-coated separator exhibit a discharge capacity of 1180, 1056, and 668 mA h g^{-1}, respectively at 0.1 C, which are 70.4%, 63.0%, and 39.8% of the theoretical value. The high-capacity utilization for Co_9S_8@HPCNS-coated separator could be attributed to the efficient capturing of the polysulfide species by the metallic and polar Co_9S_8 nanocrystals compared to nonpolar carbonaceous species in the HPCNS-coated and F-CNS-coated separators. Moreover, the hollow and porous spaces efficiently accommodated undesired volume variations during redox reactions thus inhibiting electrode pulverization. Therefore, the CV and initial charge–discharge voltage profiles confirm that the structural advantages of Co_9S_8@HPCNS resulted in an enhanced electrochemical performance.

Rate capability tests were also conducted on Li-S cells with various coated separator systems (Fig. 4c). The cell with the Co_9S_8@HPCNS-coated separator exhibited higher discharge capacities at each current rate than those of the HPCNS-coated and F-CNS-coated separators. For instance, the Co_9S_8@HPCNS-coated separator exhibited initial discharge capacities of 1180, 863, 794, 704, 605, 551, and 335 mA h g^{-1} at current rates of 0.1, 0.2, 0.3, 0.5, 0.8, 1.0, and 2.0 C, respectively. In contrast, the HPCNS-coated and F-CNS-coated separators displayed initial discharge capacities of 1056/668, 884/721, 769/664, 559/602, 394/494, 308/389, and 199/241 mA h g^{-1} at similar current rates of 0.1, 0.2, 0.3, 0.5, 0.8, 1.0, and 2.0 C, respectively. The similar discharge capacities of the Co_9S_8@HPCNS-coated and HPCNS-coated separators at low current rates were mainly attributed to the highly porous structure of the HPCNS sample that resulted in the adsorption of polysulfides to some extent. However, at high current rates, the absence of metallic and

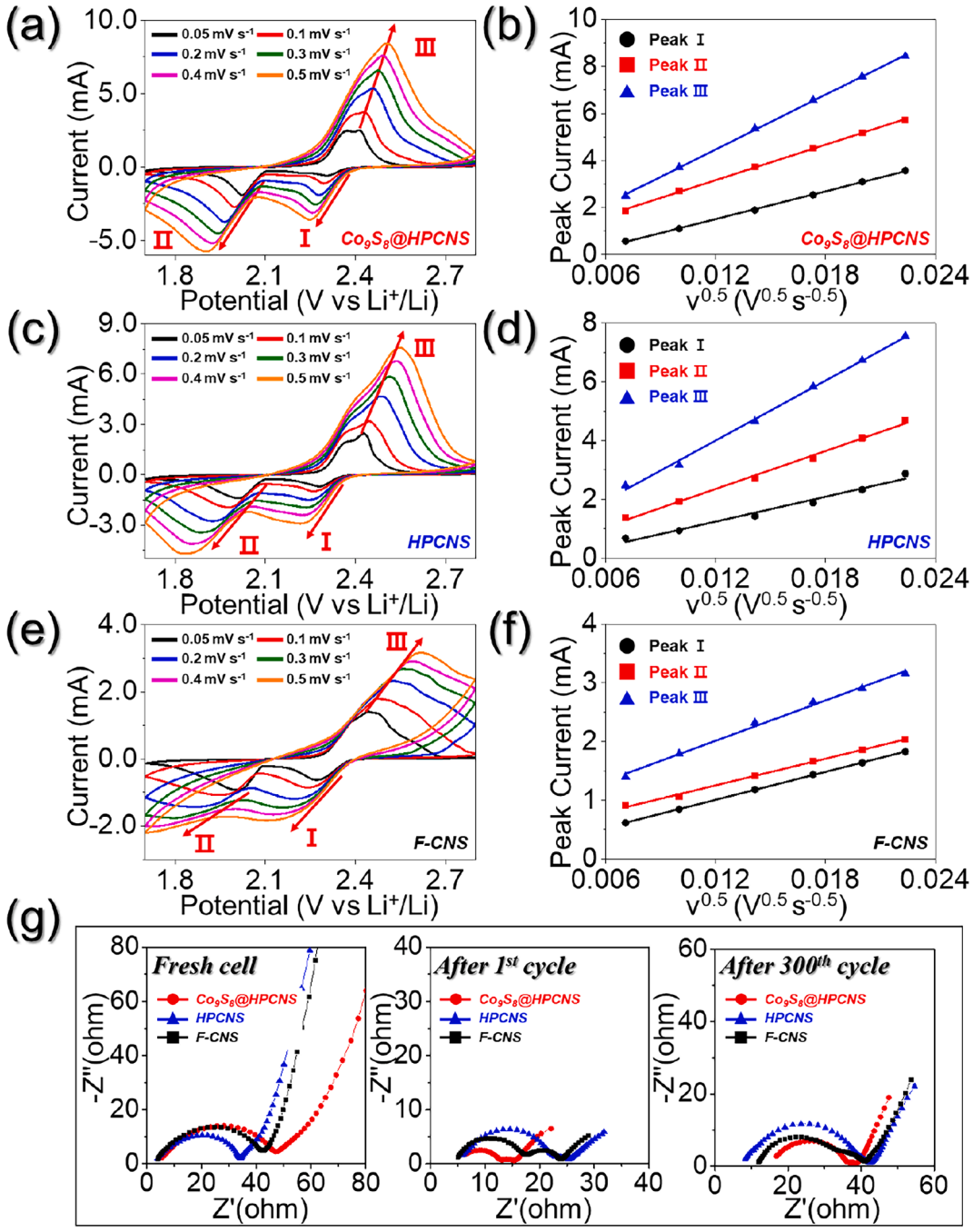

Fig. 5. Lithium–ion diffusion coefficient (D_{Li}^{+}) for the assembled Li–S cells with different interlayer arrangements: (a,c,e) cyclic voltammograms at different scan rates ranging from 0.05 to 0.5 mV s^{-1} and (b,d,f) peak current *vs.* square root of the voltage scan rate plots to calculate D_{Li}^{+}, and (g) Nyquist plots of Li-S cells cycled at 1.0 C for different cycle number.

polar species in the HPCNS resulted in poor rate capabilities. This observation is more apparent when considering capacity utilization at a high current rate. For example, the Co_9S_8@HPCNS-coated separator exhibited a capacity utilization of 20% at 2.0 C compared to 12% for the HPCNS-coated separator. This is because of the existence of several chemisorption sites in the form of polar and metallic Co_9S_8 nanocrystals, which ensure the efficient anchoring and electrocatalytic conversion of polysulfide species, thereby enhancing active material utilization. The slightly better rate performance of the Li-S cell featuring F-CNS-coated separator at high current rates compared to the HPCNS-coated separator was mainly because of the presence of micropores which were formed due to carbon shrinkage. The micropores improved active material reutilization, as reported previously [23]. The charge–discharge voltage profiles at various current rates shown in Fig. S9a–c firmly validates the above-mentioned reasoning with distinct voltage plateaus for the Co_9S_8@HPCNS-coated separator even at high current rates. Additionally, when the current direction was reversed, the cell featuring the Co_9S_8@HPCNS-coated separator fairly recovered the discharge capacities at 0.1 C, thereby confirming the structural advantages of the prepared sample.

The cycling performance was evaluated to further verify the structural merits at low and high current rates, and the results are shown in Fig. 4d and e. The cell featuring the Co_9S_8@HPCNS-coated separator exhibited an initial discharge capacity of 879 mA h g^{-1} at 0.1 C, which increased to 1081 mA h g^{-1} at the 3rd cycle mainly due to the activation process. After 250 continuous charge–discharge cycles, the cell

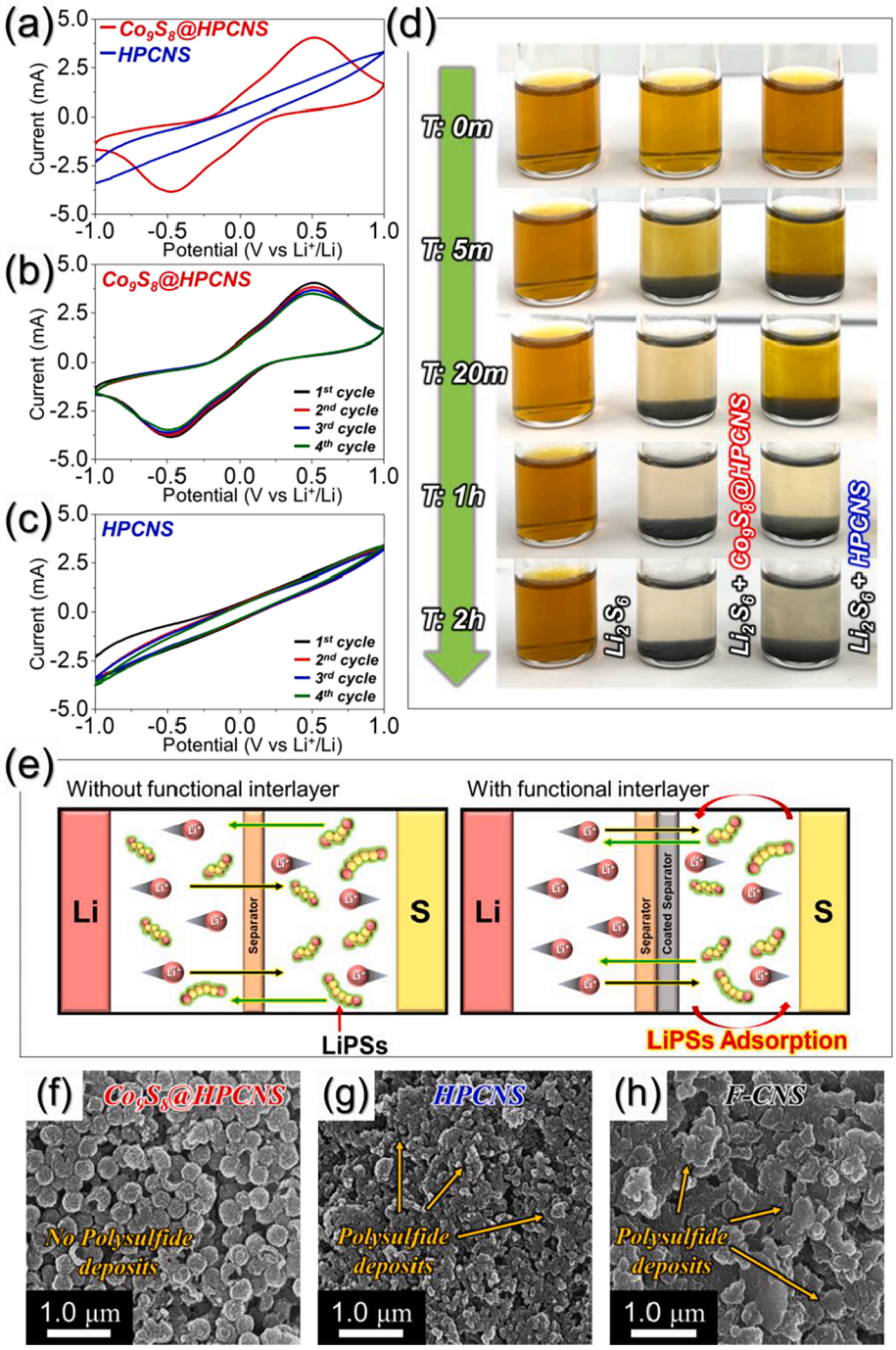

Fig. 6. (a) Initial CV profile of different symmetric cells in the voltage window of −1.0 to 1.0 V at a scan rate of 3.0 mV s^{-1}, (b, c) first four CV curves obtained using different symmetric cells arrangements, (d) Visual demonstration of polysulfide adsorption tests, (e) schematic illustration of multifunctional interlayer inhibiting the polysulfide crossover, and (f-h) post-cycling morphological changes of the cathode-side facing coated separator removed after cycling at 1.0 C-rate.

demonstrated a highly stable cycling performance, as evidenced by a discharge capacity of 656 mA h g^{-1} (75% capacity retention). This resulted in an average capacity loss of only 0.89 mA h g^{-1} per cycle. In contrast, the cell featuring the HPCNS-coated separator displayed a high initial discharge capacity of 1129 mA h g^{-1} owing to its large surface area. However, on further cycling, the capacity decreases monotonically and gets stabilized at 559 mA h g^{-1} (50% capacity retention) at the end of 250th cycle with a high-capacity loss of 2.28 mA h g^{-1} per cycle. The high-capacity retention and low-capacity loss of the Co_9S_8@HPCNS-coated separator are because of the presence of polar and metallic Co_9S_8 nanocrystals that ensure efficient polysulfide capture and facilitate their electrocatalytic conversion. In contrast, the nonpolar characteristics of the carbonaceous species in HPCNS resulted in poor polysulfide crossover suppression and, hence, continuous active material loss. Similar trends were observed for the F-CNS-coated separator, with rapidly fading capacity and low active material utilization. In addition, the high Coulombic efficiency of 100% observed for the Co_9S_8@HPCNS-coated separator at the end of 250 cycles indicated highly reversible electrochemical processes. Similarly, at a high current rate of 1.0 C (Fig. 4e), the cells featuring the Co_9S_8@HPCNS-coated separator exhibit better cycling performances than those containing the HPCNS-coated and F-CNS-coated separators. For instance, a discharge capacity of 395 mA h

g^{-1} (70% retention after the 7th cycle) was obtained after 300 cycles with an average capacity loss of 0.56 mA h g^{-1} per cycle. In contrast, the HPCNS-coated and F-CNS-coated separators displayed low discharge capacities of 251 and 277 mA h g^{-1}, respectively, after an identical number of cycles. The prolonged cycling of the Co_9S_8@HPCNS-coated separator at 0.5 C (Fig. S10) agrees well with the aforementioned results. It should be noted that the average discharge capacity error associated with different cells was around ± 5 mA h g^{-1}. The performance of electrocatalytic interlayers in the present work is comparable to the previously reported results on various interlayer materials, as shown in Table S1. The practical feasibility of the as-prepared Co_9S_8@HPCNS sample as a multifunctional interlayer was further verified using high-loading electrodes, as shown in Fig. S11a and b. The cell with an active loading of 2.0 mg cm^{-2} exhibited a highly stable cycling performance at 0.3 C with a final discharge capacity of 321 mA h g^{-1} after 1000 cycles (58% capacity retention measured from the 5th cycle and a capacity loss of only 0.23 mA h g^{-1} per cycle). When the mass loading was further improved to 3.2 mg cm^{-2} (S content = 57 wt%), the cell maintained its cycling stability for 300 cycles, with a final discharge capacity of 391 mA h g^{-1}. However, the initial increase in the discharge capacity is mainly because of the activation of the active material, as previously reported [2]. These results prove that the structural advantages of the Co_9S_8@HPCNS sample facilitate kinetically favored redox processes with rapid electron transfer and smooth charge-diffusion characteristics. Furthermore, the poor rate capability and inferior cycling performance (at 1.0 C) of the pristine Co_9S_8 sample in Fig. S12 again validate the structural merits of Co_9S_8@HPCNS sample.

To validate the charge-diffusion properties of all the assembled cells incorporating different separator configurations, the Li-ion diffusion coefficient (D_{Li}^{+}) was determined using CV curves in a voltage range of 1.7–2.8 V at different scan rates of 0.05–0.5 mV s^{-1}, and the results are presented in Fig. 5. The CV curves obtained at various voltage scan rates exhibited standard Li–S redox peaks, suggesting that the electrochemical processes inside the cells were similar to those between elemental S and Li_2S. However, compared with that of other cells, the high current values were observed for the cell with the Co_9S_8@HPCNS-coated separator (Fig. 5a), even at a high voltage ramp rate of 0.5 mV s^{-1}, indicating rapid redox processes and the efficient diffusion of charge carriers. The well-known Randles–Sevcik equation was further applied to calculate the D_{Li}^{+} values for each cell [8]:

$$I_p = (2.69 \times 10^5) n^{1.5} A D_{Li^+}^{0.5} C_{Li} \nu^{0.5} \quad (1)$$

where I_p represents the current values for various redox peak; n quantify the involved electrons in the redox reaction ($n = 2$); A is the electrode area (cm^2); C_{Li} is the concentration of Li-ion (mol L^{-1}); and ν is the voltage ramp rate (V s^{-1}). The I_p *vs.* $\nu^{0.5}$ plots obtained for Li–S cells with the Co_9S_8@HPCNS-coated, HPCNS-coated, and F-CNS-coated separators are shown in Fig. 5b, d, and f, respectively, and the corresponding D_{Li}^{+} values are listed in Table 1. The cell featuring the Co_9S_8@HPCNS-coated separator exhibited the highest D_{Li}^{+} values, indicating excellent diffusion processes inside the cell compared to other assembled cells. The D_{Li}^{+} values confirm that the synergetic effects of the polar Co_9S_8 nanocrystals and the hollow nanostructure improved the overall electrochemical performance of Co_9S_8@HPCNS compared to that of the HPCNS.

The improved redox reaction processes inside the assembled Li–S cells were further confirmed by Nyquist plot assessment (Fig. 5g). In addition, the equivalent circuit model comprising all fitted impedance parameters for Li–S cells with various coated separators is presented in Fig. S13. The impedance was determined at an open-circuit potential for all Li–S cells at various cycles during cycling at 1.0 C. All Li–S fresh cells exhibited similar electrolyte resistance (R_e) values, implying a stable separator–electrolyte–electrode interfacial boundary. Furthermore, the fresh Li–S cell with the HPCNS-coated separator exhibited the smallest charge transfer impedance (R_{ct}; ~32 Ω) because of the highly porous structure of the HPCNS sample compared with that of Co_9S_8@HPCNS (~45 Ω) and F-CNS (~41 Ω). However, after the 1st cycle, the Co_9S_8@HPCNS-coated separator exhibited the lowest total cell resistance (~12 Ω), compared with that of the HPCNS-coated (~21 Ω) and F-CNS-coated (~20 Ω) separators. Even after 300 cycles, the Li–S cell with the Co_9S_8@HPCNS-coated separator displayed the lowest total cell resistance value of 25 Ω compared to the HPCNS-coated (35 Ω) and F-CNS-coated (31 Ω) separators. Additionally, the appearance of two well-distinguished semicircles for the F-CNS-coated separator indicates inferior Li-ion diffusion compared to that of the others owing to the formation of nonconducting deposits of Li_2S_2 or Li_2S, as previously reported [50]. This observation is consistent with the cycling performance results of the Li-S cell pairing the F-CNS-coated separator, as indicated in Fig. 4. These results further advocate that the structural supremacy of the Co_9S_8@HPCNS-coated separator compared to that of the other analyzed separators ensures kinetically preferred redox reactions inside the cell and enhances the structural integrity of the sulfur electrode during extended cycling and efficient polysulfide anchoring.

To investigate the effect of the electrocatalytic anchoring of lithium polysulfide using the Co_9S_8@HPCNS-coated separator, CV curves were obtained *via* symmetrical cells with the as-prepared nanospheres as the counter and working electrodes, which were further penetrated with the polysulfide solution, as presented in Fig. 6. The initial CV profile for symmetrical cells is obtained at a voltage ramp rate of 3.0 mV s^{-1}, with the voltage ranging from –1.0 to 1.0 V (Fig. 6a). The CV curves exhibit appreciable differences as the Co_9S_8@HPCNS symmetrical cell exhibits an effective electrocatalytic nature toward polysulfides, as evidenced by the intense current peaks. In contrast, the HPCNS symmetrical cell exhibits low electrocatalytic performance toward polysulfides, owing to the absence of active chemisorption sites in the prepared nanospheres. Furthermore, the CV plots for four successive cycles shown in Fig. 6b and c display almost overlapping curves, suggesting effective catalytic anchoring at different scales. These interpretations are further confirmed by visual polysulfide adsorption experiments (Fig. 6d). The adsorption of lithium polysulfide was attributed to Co_9S_8@HPCNS, as evidenced by a continuous change in the color of the polysulfide solution from pale yellow (at T = 0) to almost clear (T = 2 h). The solution containing HPCNS also exhibited similar polysulfide adsorption characteristics, which could be attributed to the highly porous structure of the sample. Furthermore, the XPS profiles of interlayer materials were also analyzed after cycling for the S 2p photoelectron signal, as shown in Fig. S14. The existence of a photoelectron peak at binding energy of 166.9 eV for the cycled Co_9S_8@HPCNS and HPCNS sample is designated to the thiosulfate ($-S_2O_3^{2-}$) groups, which is usually considered as an indication of the surface redox reaction between the polysulfide and polar species [51]. This phenomenon resulted in the effective mitigation of higher-order polysulfide migration by converting them to insoluble lower-order polysulfides. The sharp peak at 168.6 eV is related to the polythionate complexes which formed due to the reaction of elemental S with nucleophilic species such as HS^- or SO_3^{2-} [51]. The high intensity of polythionate complex peak for cycled Co_9S_8@HPCNS compared to HPCNS simply indicates better polysulfide anchoring. The fitted peak at 169.9 eV is ascribed to the sulfate ($-SO_4^{2-}$) species that originated due to LiTFSI decomposition inside the cell, which is considered as a key source of Li_xSO_y species [52]. These findings confirm that the structural advantages of Co_9S_8@HPCNS result in the efficient capture and conversion of the polysulfide species, owing to the availability of metallic and polar

Table 1
The Li–ion diffusion coefficient results (D_{Li}^{+}) for the Li–S cells featuring different separator arrangements.

Sample	D_{Li+} (cm^2 s^{-1}) × 10^{-8}			Avg. D_{Li+} (cm^2 s^{-1}) × 10^{-8}
	Peak I	Peak II	Peak III	
Co_9S_8@HPCNS	2.82	4.60	11.0	6.14
HPCNS	1.45	3.39	8.47	4.43
F-CNS	0.46	0.42	0.96	0.61

Co_9S_8 nanocrystals as chemisorption sites (Fig. 6e).

To further validate the structural integrity of the Co_9S_8@HPCNS sample, the cells were carefully disassembled after 300 cycles at 1.0 C, and SEM micrographs of the coated separators were obtained, as shown in Fig. 6f–h. The SEM micrographs of the coated separator with Co_9S_8@HPCNS (Fig. 6f) show that the spherical morphology remains unchanged even after extended cycling, indicating the high structural robustness of the nanostructure. In addition, no polysulfide accumulations are observed, indicating the efficient electrocatalytic transformation of sulfur-like species. In contrast, the cells with the HPCNS-coated (Fig. 6g) and F-CNS-coated (Fig. 6h) separators show enormous polysulfide sediments, implying a weak catalytic transformation effect because of the lack of redox-active species and the nonpolar nature of the carbonaceous species in the nanostructure.

Overall, the introduction of a multifunctional interlayer in the form of a Co_9S_8@HPCNS-coated separator placed on the cathode side resulted in enhanced electrochemical properties such as sufficient rate capabilities and prolonged cycling stabilities at various C rates. The porous nanostructure ensured rapid charge diffusion and improved electrolyte percolation, resulting in an improved cell performance. Additionally, the presence of metallic and polar Co_9S_8 nanocrystals facilitated the effective catalytic conversion of trapped polysulfide species, resulting in high sulfur utilization. Therefore, we anticipate that the synthesis strategy discussed herein will substantially enhance the current knowledge on the development of advanced nanostructures.

4. Conclusions

In summary, we analyzed the electrochemical performance of Li–S cells using a modified cell component as a coating separator. The coated separator consists of hollow porous carbon nanospheres (HPCNSs) comprising well-embedded metallic and polar Co_9S_8 nanocrystals (abbreviated as Co_9S_8@HPCNS). Initially, the HPCNS sample was prepared *via* facile polymerization followed by carbonization and template removal. Subsequently, the Co_9S_8 nanocrystals were impregnated inside the HPCNS using a drop and dry method. The as-prepared Co_9S_8@HPCNS sample was then used as a multifunctional and electrocatalytic interlayer for highly stable LSBs. The porous nanostructure of the multifunctional barrier facilitated rapid charge diffusion and efficient electrolyte infiltration. In addition, the well-grafted metallic and polar cobalt sulfide (Co_9S_8) nanocrystals served as chemisorption sites for efficient polysulfide anchoring and prevented migration toward the anode *via* efficient catalytic conversion, thereby increasing sulfur utilization. The prepared Li–S cell with regular S electrode and Co_9S_8@HPCNS interlayer as a polysulfide barrier demonstrated an overall enhanced electrochemical property in comparison with the literature, such as good rate capability (335 mA h g^{-1} at 2.0 C) and long-term stability (395 mA h g^{-1} at 1.0 C rate after 300 cycles) [53–55]. Even with a high S loading (3.2 mg cm^{-2}) and S content (57 wt%), the cell featuring a Co_9S_8@HPCNS-coated separator exhibited significantly high electrochemical performance (391 mA h g^{-1} after 300 cycles at a 0.3 C rate). Therefore, we anticipate that the physical and electrochemical results presented herein will provide crucial insights into the expansion of porous and conductive nanostructures as host or interlayer material for several energy storage purposes.

CRediT authorship contribution statement

Su Hyun Yang: Conceptualization, Methodology. **Jang Min Choi:** Data curation. **Rakesh Saroha:** Visualization, Preparation of original draft. **Sung Woo Cho:** Carried out experiments. **Yun Chan Kang:** Supervision. **Jung Sang Cho:** Writing – review & editing, Supervision.

Declaration of Competing Interest

The authors declare that they have no known competing financial interests or personal relationships that could have appeared to influence the work reported in this paper.

Data availability

No data was used for the research described in the article.

Acknowledgments

This work was supported by the National Research Foundation of Korea (NRF), funded by the Korean government (MSIP) [grant numbers NRF-2021R1A4A2001687 and NRF-2021R1I1A3057700].

Appendix A. Supplementary data

Supplementary data to this article can be found online at https://doi.org/10.1016/j.jcis.2023.04.083.

References

[1] R. Liu, F. Guo, X. Zhang, J. Yang, M. Li, W. Miaomiao, H. Liu, M. Feng, L. Zhang, Novel "bird-nest" structured Co_3O_4/acidified multiwall carbon nanotube (ACNT) hosting materials for lithium–sulfur batteries, ACS Appl. Energy Mater. 2 (2019) 1348–1356.
[2] R. Saroha, J.S. Cho, Nanofibers comprising interconnected chain-like hollow N-doped c nanocages as 3D free-standing cathodes for Li–S batteries with super-high sulfur content and lean electrolyte/sulfur ratio, Small Methods (2022) 2200049.
[3] X. Yu, A. Manthiram, A class of polysulfide catholytes for lithium–sulfur batteries: energy density, cyclability, and voltage enhancement, Phys. Chem. Chem. Phys. 17 (2015) 2127–2136.
[4] R. Saroha, J.-H. Ahn, J.S. Cho, A short review on dissolved lithium polysulfide catholytes for advanced lithium-sulfur batteries, Korean J. Chem. Eng. 38 (2021) 461–474.
[5] R. Saroha, J.S. Cho, J.-H. Ahn, Synergetic effects of cation (K+) and anion (S2−)-doping on the structural integrity of Li/Mn-rich layered cathode material with considerable cyclability and high-rate capability for Li-ion batteries, Electrochim. Acta 366 (2021) 137471.
[6] J.S. Lee, J.-S. Park, K.W. Baek, R. Saroha, S.H. Yang, Y.C. Kang, J.S. Cho, Coral-like porous microspheres comprising polydopamine-derived N-doped C-coated $MoSe_2$ nanosheets composited with graphitic carbon as anodes for high-rate sodium-and potassium-ion batteries, Chem. Eng. J. 456 (2023) 141118.
[7] R.D. Rauh, K.M. Abraham, G.F. Pearson, J.K. Surprenant, S.B. Brummer, A lithium/dissolved sulfur battery with an organic electrolyte, J. Electrochem. Soc. 126 (1979) 523.
[8] R. Saroha, J.H. Oh, Y.H. Seon, Y.C. Kang, J.S. Lee, J.S. Cho, Freestanding interlayers for Li–S batteries: design and synthesis of hierarchically porous N-doped C nanofibers comprising vanadium nitride quantum dots and MOF-derived hollow N-doped C nanocages, J. Mater. Chem. A 9 (2021) 11651–11664.
[9] Q. Wu, X. Zhou, J. Xu, F. Cao, C. Li, Carbon-based derivatives from metal-organic frameworks as cathode hosts for Li–S batteries, J. Energy Chem. 38 (2019) 94–113.
[10] R. Saroha, J. Heo, Y. Liu, N. Angulakshmi, Y. Lee, K.-K. Cho, H.-J. Ahn, J.-H. Ahn, V_2O_3-decorated carbon nanofibers as a robust interlayer for long-lived, high-performance, room-temperature sodium–sulfur batteries, Chem. Eng. J. 431 (2022) 134205.
[11] R. Saroha, J.H. Oh, J.S. Lee, Y.C. Kang, S.M. Jeong, D.-W. Kang, C. Cho, J.S. Cho, Hierarchically porous nanofibers comprising multiple core–shell Co_3O_4@graphitic carbon nanoparticles grafted within N-doped CNTs as functional interlayers for excellent Li–S batteries, Chem. Eng. J. 426 (2021) 130805.
[12] R. Saroha, Y.H. Seon, B. Jin, Y.C. Kang, D.-W. Kang, S.M. Jeong, J.S. Cho, Self-supported hierarchically porous 3D carbon nanofiber network comprising Ni/Co/$NiCo_2O_4$ nanocrystals and hollow N-doped C nanocages as sulfur host for highly reversible Li–S batteries, Chem. Eng. J. 137141 (2022).
[13] Q. Pang, D. Kundu, M. Cuisinier, L. Nazar, Surface-enhanced redox chemistry of polysulphides on a metallic and polar host for lithium-sulphur batteries, Nat. Commun. 5 (2014) 4759.
[14] Y.H. Seon, R. Saroha, J.S. Cho, Hierarchically porous N-doped C nanofibers comprising TiO_2 quantum dots and ZIF-8-derived hollow C nanocages as ultralight interlayer for stable Li–S batteries, Compos. B: Eng. 237 (2022) 109856.
[15] R. Saroha, J. Heo, X. Li, N. Angulakshmi, Y. Lee, H.-J. Ahn, J.-H. Ahn, J.-H. Kim, Asymmetric separator integrated with ferroelectric-$BaTiO_3$ and mesoporous-CNT for the reutilization of soluble polysulfide in lithium-sulfur batteries, J. Alloys Compd. 893 (2022) 162272.
[16] J.M. Choi, R. Saroha, J.S. Kim, M.R. Jang, J.S. Cho, Porous nanofibers comprising VN nanodots and densified N-doped CNTs as redox-active interlayers for Li–S batteries, J. Power Sources 559 (2023) 232632.
[17] L. Fan, M. Li, X. Li, W. Xiao, Z. Chen, J. Lu, Interlayer Material Selection for Lithium-Sulfur Batteries, Joule 3 (2019) 361–386.
[18] E.N. Chiristina, S.U. Rahayu, A. Tubtimtae, J.-B. Shi, M.-W. Lee, Rare-earth-incorporated ternary $Ce_xCd_{1-x}S$ quantum dot-sensitized solar cells, RSC Adv. 12 (2022) 31093–31101.

[19] M. Wang, X. Xia, Y. Zhong, J. Wu, R. Xu, Z. Yao, D. Wang, W. Tang, X. Wang, J. Tu, Porous carbon hosts for lithium–sulfur batteries, Chem. Eur. J. 25 (2019) 3710–3725.

[20] M.H. Yap, K.L. Fow, G.Z. Chen, Synthesis and applications of MOF-derived porous nanostructures, Green, Energy Environ. 2 (2017) 218–245.

[21] S.-H. Chung, C.-H. Chang, A. Manthiram, A carbon-cotton cathode with ultrahigh-loading capability for statically and dynamically stable lithium–sulfur batteries, ACS Nano 10 (2016) 10462–10470.

[22] Z. Li, Y. Jiang, L. Yuan, Z. Yi, C. Wu, Y. Liu, P. Strasser, Y. Huang, A highly ordered meso@ microporous carbon-supported sulfur@ smaller sulfur core–shell structured cathode for Li–S batteries, ACS Nano 8 (2014) 9295–9303.

[23] Y.-S. Su, A. Manthiram, Lithium–sulphur batteries with a microporous carbon paper as a bifunctional interlayer, Nat. Commun. 3 (2012) 1166.

[24] L. Zhou, H. Li, X. Wu, Y. Zhang, D.L. Danilov, R.-A. Eichel, P.H. Notten, Double-shelled Co_3O_4/C nanocages enabling polysulfides adsorption for high-performance lithium–sulfur batteries, ACS Appl. Energy Mater. 2 (2019) 8153–8162.

[25] G. Liang, J. Wu, X. Qin, M. Liu, Q. Li, Y.-B. He, J.-K. Kim, B. Li, F. Kang, Ultrafine TiO_2 decorated carbon nanofibers as multifunctional interlayer for high-performance lithium–sulfur battery, ACS Appl. Mater. Interfaces 8 (2016) 23105–23113.

[26] Z. Sun, J. Zhang, L. Yin, G. Hu, R. Fang, H.-M. Cheng, F. Li, Conductive porous vanadium nitride/graphene composite as chemical anchor of polysulfides for lithium-sulfur batteries, Nat. Commun. 8 (2017) 1–8.

[27] Z. Ren, Z. Zhao, K. Zhang, X. Wang, Y. Wang, Electrochemical behavior promotion of polysulfides by cobalt selenide/carbon cloth interlayer in lithium−sulfur batteries, ChemElectroChem 8 (2021) 1531–1536.

[28] B. Wang, D. Sun, Y. Ren, X. Zhou, Y. Ma, S. Tang, X. Meng, MOFs derived ZnSe/N-doped carbon nanosheets as multifunctional interlayers for ultralong-life lithium-sulfur batteries, J. Mater. Sci. Technol. 125 (2022) 97–104.

[29] M.S. Kim, L. Ma, S. Choudhury, S.S. Moganty, S. Wei, L.A. Archer, Fabricating multifunctional nanoparticle membranes by a fast layer-by-layer Langmuir-Blodgett process: Application in lithium–sulfur batteries, J. Mater. Chem. A 4 (2016) 14709–14719.

[30] J. Li, C. Jiao, J. Zhu, L. Zhong, T. Kang, S. Aslam, J. Wang, S. Zhao, Y. Qiu, Hybrid co-based MOF nanoboxes/CNFs interlayer as microreactors for polysulfides-trapping in lithium-sulfur batteries, J. Energy Chem. 57 (2021) 469–476.

[31] Y. Ning, B. Wang, F. Jin, J. Yang, J. Zhang, H. Luo, F. Wu, Z. Zhang, H. Zhang, Y. Zhou, D. Wang, A rational VO_2 nanotube/graphene binary sulfur host for superior lithium-sulfur batteries, J. Alloys Compd. 838 (2020) 155504.

[32] M. Barghamadi, A.S. Best, A.I. Bhatt, A.F. Hollenkamp, M. Musameh, R.J. Rees, T. Rüther, Lithium–sulfur batteries—the solution is in the electrolyte, but is the electrolyte a solution? Energy Environ. Sci. 7 (2014) 3902–3920.

[33] P. Chongngam, A. Tubtimtae, Structural, optical, and electrochemical characteristics of undoped and In^{3+}-doped tin antimony sulfide thin films for device applications, J. Mater. Sci.: Mater. Electron. 34 (2023) 71.

[34] J.S. Cho, J.M. Won, J.-H. Lee, Y.C. Kang, Synthesis and electrochemical properties of spherical and hollow-structured NiO aggregates created by combining the Kirkendall effect and Ostwald ripening, Nanoscale 7 (2015) 19620–19626.

[35] C.S. Kim, J.S. Lee, R. Saroha, Y.B. Park, Y.C. Kang, D.-W. Kang, S.M. Jeong, J. S. Cho, Porous nitrogen-doped graphene nanofibers comprising metal organic framework-derived hollow and ultrafine layered double metal oxide nanocrystals as high-performance anodes for lithium-ion batteries, J. Power Sources 523 (2022) 231030.

[36] J.S. Lee, R. Saroha, J.S. Cho, Porous microspheres comprising $CoSe_2$ nanorods coated with N-doped graphitic C and polydopamine-derived C as anodes for long-lived Na-ion batteries, Nano Micro Lett. 14 (2022) 1–22.

[37] B. Dong, J.-Y. Xie, N. Wang, W.-K. Gao, Y. Ma, T.-S. Chen, X.-T. Yan, Q.-Z. Li, Y.-L. Zhou, Y.-M. Chai, Zinc ion induced three-dimensional Co_9S_8 nano-neuron network for efficient hydrogen evolution, Renew, Energ. 157 (2020) 415–423.

[38] X. Chen, R. Jiang, C. Dong, H. Liu, J. Yang, X. Du, Polycrystalline CoO−Co_9S_8 heterostructure nanoneedle arrays as bifunctional catalysts for efficient overall water splitting, ChemElectroChem 9 (2022) e202101566.

[39] K. Zhao, Y. Zhao, M. Hao, X. Li, S. Liu, L. Li, W. Zhang, Cost effective synthesis Co_9S_8/Ni_9S_8 loaded on nitrogen doped porous carbons high efficiency counter electrode materials for liquid thin film solar cells, Electrochim. Acta 399 (2021) 139441.

[40] W. Lin, G. He, Y. Huang, X. Chen, 3D hybrid of Co_9S_8 and N-doped carbon hollow spheres as effective hosts for Li-S batteries, Nanotechnology 31 (2019) 035404.

[41] X. Zhu, Q. Wu, J. Dai, D. Zhao, C. Yang, L. Li, N. Li, S. Chen, Co_9S_8 nanoparticles embedded in nitrogen, sulfur codoped porous carbon nanosheets for efficient oxygen/hydrogen electrocatalysis, Electrochim. Acta 384 (2021) 138299.

[42] H. Liu, C.-Y. Xu, Y. Du, F.-X. Ma, Y. Li, J. Yu, L. Zhen, Ultrathin Co_9S_8 nanosheets vertically aligned on N, S/rGO for low voltage electrolytic water in alkaline media, Sci. Rep. 9 (2019) 1–10.

[43] J.S. Lee, R. Saroha, S.H. Oh, D.H. Shin, S.M. Jeong, J.K. Kim, J.S. Cho, Rational design of perforated bimetallic (Ni, Mo) sulfides/N-doped graphitic carbon composite microspheres as anode materials for superior Na-ion batteries, Small Methods 5 (2021) 2100195.

[44] J.S. Lee, R. Saroha, J.H. Oh, C. Cho, B. Jin, D.-W. Kang, J.S. Cho, Camphene-derived hollow and porous nanofibers decorated with hollow NiO nanospheres and graphitic carbon as anodes for efficient lithium-ion storage, J. Ind. Eng. Chem. 114 (2022) 276–287.

[45] R. Saroha, H.S. Ka, J.S. Cho, A novel three-dimensional ordered mesoporous microspheres comprising N-doped graphitic carbon-coated Fe_xP nanoparticles as multifunctional interlayers to suppress polysulfide crossover in Li–S batteries, Appl. Surf. Sci. 612 (2022) 155892.

[46] S.H. Oh, S.M. Park, D.-W. Kang, Y.C. Kang, J.S. Cho, Fibrous network of highly integrated carbon nanotubes/MoO_3 composite bundles anchored with MoO_3 nanoplates for superior lithium-ion battery anodes, J. Ind. Eng. Chem. 83 (2020) 438–448.

[47] G. Ma, X. Xu, Z. Feng, C. Hu, Y. Zhu, X. Yang, J. Yang, Y. Qian, Carbon-coated mesoporous Co_9S_8 nanoparticles on reduced graphene oxide as a long-life and high-rate anode material for potassium-ion batteries, Nano Res. 13 (2020) 802–809.

[48] R. Saroha, A.K. Panwar, Effect of in situ pyrolysis of acetylene (C_2H_2) gas as a carbon source on the electrochemical performance of $LiFePO_4$ for rechargeable lithium-ion batteries, J. Phys. D: Appl. Phys. 50 (2017) 255501.

[49] C. Zhang, K.B. Hatzell, M. Boota, B. Dyatkin, M. Beidaghi, D. Long, W. Qiao, E. C. Kumbur, Y. Gogotsi, Highly porous carbon spheres for electrochemical capacitors and capacitive flowable suspension electrodes, Carbon 77 (2014) 155–164.

[50] Z.A. Ghazi, X. He, A.M. Khattak, N.A. Khan, B. Liang, A. Iqbal, J. Wang, H. Sin, L. Li, Z. Tang, MoS_2/celgard separator as efficient polysulfide barrier for long-life lithium–sulfur batteries, Adv. Mater. 29 (2017) 1606817.

[51] X. Liang, C. Hart, Q. Pang, A. Garsuch, T. Weiss, L.F. Nazar, A highly efficient polysulfide mediator for lithium–sulfur batteries, Nat. Commun. 6 (2015) 1–8.

[52] V. Sharova, A. Moretti, T. Diemant, A. Varzi, R.J. Behm, S. Passerini, Comparative study of imide-based Li salts as electrolyte additives for Li-ion batteries, J. Power Sources 375 (2018) 43–52.

[53] W. Tong, Y. Huang, W. Jia, X. Wang, Y. Guo, Z. Sun, D. Jia, J. Zong, Leaf-like interconnected network structure of MWCNT/Co_9S_8/S for lithium-sulfur batteries, J. Alloys Compd. 731 (2018) 964–970.

[54] H. Zhang, J. Ma, M. Huang, H. Shang, J. Jiang, Y. Qiao, W. Liu, H. Zhou, T. Li, X. Zhou, G. Peng, M. Ye, M. Qu, MOF-derived Co_9S_8/C hollow polyhedra grown on 3D graphene aerogel as efficient polysulfide mediator for long-life Li-S batteries, Mater. Lett. 277 (2020) 128331–128334.

[55] J. Wei, H. Su, C. Qin, B. Chen, H. Zhang, J. Wang, Multifunctional Co_9S_8 nanotubes for high-performance lithium-sulfur batteries, J. Electroanal. Chem. 837 (2019) 184–190.